

1 **Plasmonic Anapole Metamaterial for Refractive Index Sensing**

2 Jin Yao^{1,‡}, Jun-Yu Ou^{2,‡}, Vassili Savinov², Mu Ku Chen^{1,3,4}, Hsin Yu Kuo², Nikolay I.
3 Zheludev^{2,5,*}, and Din Ping Tsai^{1,3,4,*}

4

5 ¹*Department of Electrical Engineering, City University of Hong Kong, Kowloon, Hong
6 Kong SAR, China.*

7 ²*Optoelectronics Research Centre and Centre for Photonic Metamaterials, University of
8 Southampton, Highfield, Southampton SO17 1BJ, United Kingdom.*

9 ³*Centre for Biosystems, Neuroscience, and Nanotechnology, City University of Hong Kong,
10 Kowloon, Hong Kong SAR, China.*

11 ⁴*The State Key Laboratory of Terahertz and Millimeter Waves, City University of Hong
12 Kong, Kowloon, Hong Kong SAR, China.*

13 ⁵*Centre for Disruptive Photonic Technologies, SPMS, TPI, Nanyang Technological
14 University, Singapore 637371, Singapore.*

15

16 ‡These authors contributed equally to this work.

17 *E-mail: zheludev@soton.ac.uk and dptsai@cityu.edu.hk

18

19

20

21

22

23

24 **Abstract**

25 Anapole mode is a nonradiative state of light originating from the interference of electric
26 and toroidal dipole moments, accompanied by nontrivial field confinement and
27 enhancement. High-quality anapole-related resonances can be used in enhancing nonlinear
28 electromagnetic properties of materials and in sensor applications. Spectroscopy of
29 anapoles presents considerable challenges due to weak coupling to free-space
30 electromagnetic waves, but it is also an advantage for sensing. In this work, we
31 experimentally demonstrate the first plasmonic anapole metamaterial sensor of
32 environmental refractive index in the optical part of the spectrum. Our results show that
33 the plasmonic anapole metamaterial possesses high sensitivity to the ambient refractive
34 index with the sensitivity of 330 nm/RIU and 445 nm/RIU in experiment and simulation,
35 respectively. The experimental detection limit of 8.7×10^{-5} RIU is obtained as well. This
36 work will pave the way for tailoring and controlling the anapole mode and will facilitate
37 many significant applications in biosensing and spectroscopy.

38

39 **Keywords:** plasmonic metamaterial, anapole mode, refractive index sensor, vertical split-
40 ring resonator, toroidal dipole

41

42

43

44

45

46

47 **Introduction**

48 Refractive index sensing has attracted extensive attention due to a wide range of chemical
49 and biomedical applications [1, 2]. In recent years, plasmonic metamaterials and
50 metasurfaces have emerged as powerful candidates for novel refractive index sensors [3-
51 7]. They possess preeminent capabilities of confining the electromagnetic field at the
52 nanoscale and enhancing the interactions between light and matter, providing high
53 sensitivity to the ambient refractive index variations [8, 9]. Propagating surface plasmon
54 polariton (SPP) and localized surface plasmon resonance (LSPR) are among the most
55 common plasmonic refractive index sensing techniques [10-12]. By carefully engineering
56 and optimizing the nanostructure designs, performant plasmonic sensors with high
57 sensitivity, high figure-of-merit (FOM) and low detection limit have been achieved [13-
58 15]. Beyond this, the research attention has focused on the interplays between resonant
59 modes, such as Fano resonances and quasi-bound states in the continuum. Excellent near-
60 field enhancement and Q factor have been demonstrated, potentially enabling great
61 performance in label-free and real-time sensing applications [16-21].

62 Anapole mode is a nonradiative resonance that arises as a result of the destructive
63 interference between electric dipole (ED) and toroidal dipole (TD) moments with the same
64 intensity and opposite phase in the far-field [22, 23]. The anapole excitation was first
65 experimentally observed within engineered composite metallic metamaterials at
66 microwave frequency [24]. It was then extended to plasmonic and dielectric metamaterials
67 and metasurfaces in the infrared [25-28]. The generalizations of the electric anapole modes
68 such as the high-order anapole states and the magnetic counterparts have also been studied
69 [29]. The defining nonradiating condition of the anapole relies on the fine balance between

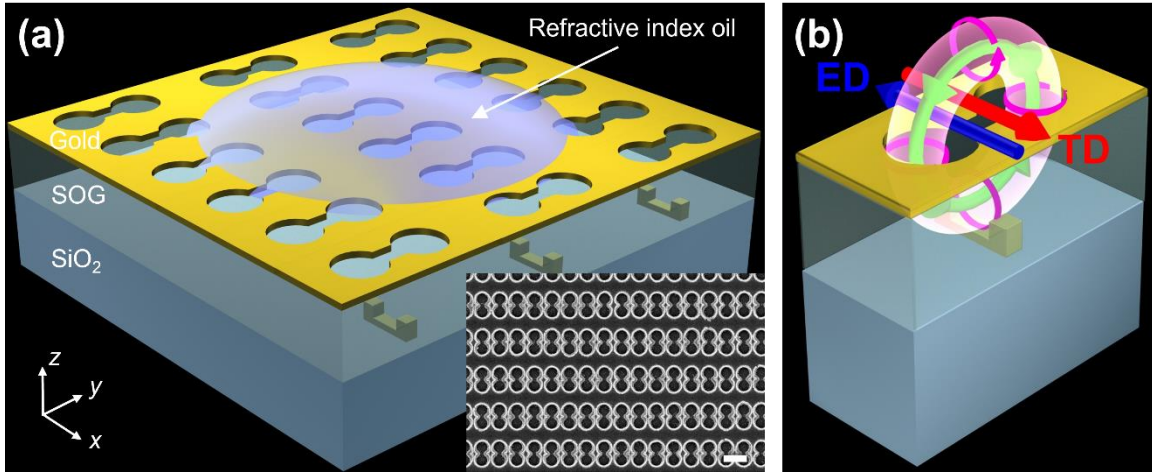
70 the constituent electric dipole and toroidal dipole excitations. Consequently, such
71 excitations are expected to be highly sensitive to external perturbations including variations
72 in the ambient refractive index [30-32]. Compared with conventional dipole modes with
73 low transmission, anapole modes can acquire the effective transmission channel due to the
74 nonradiative property, which is beneficial to practical low-loss sensors [25, 33]. Leveraging
75 this intuition, various enhanced anapole modes and their great sensing performance have
76 been demonstrated in dielectric nanostructures with high refractive index. In contrast, few
77 studies have touched on plasmonic anapole sensing so far, and the experimental
78 demonstration of the plasmonic anapole metamaterial sensor remains unexplored in the
79 optical part of the spectrum. [34-38].

80 In this work, we experimentally demonstrate the first plasmonic anapole sensor for
81 refractive index sensing in the optical part of spectrum. By comparing the electromagnetic
82 responses of electric dipole and toroidal dipole, we investigate the physical mechanism of
83 the anapole excitation. Due to the effective coupling between two components, we acquire
84 a higher field enhancement and a narrower linewidth of the whole plasmonic anapole
85 metamaterial, which can improve the refractive index sensing performance. We further
86 numerically and experimentally demonstrate the high sensitivity of the plasmonic
87 refractive index sensor. Simultaneously, for the first time, we demonstrate tuning of the
88 anapole excitation through control of the ambient refractive index.

89

90 **Results and discussion**

91 Figure 1a depicts the schematic diagram of the proposed plasmonic anapole metamaterial,
92 which consists of a planar array of vertical split-ring resonators suspended in a spin on



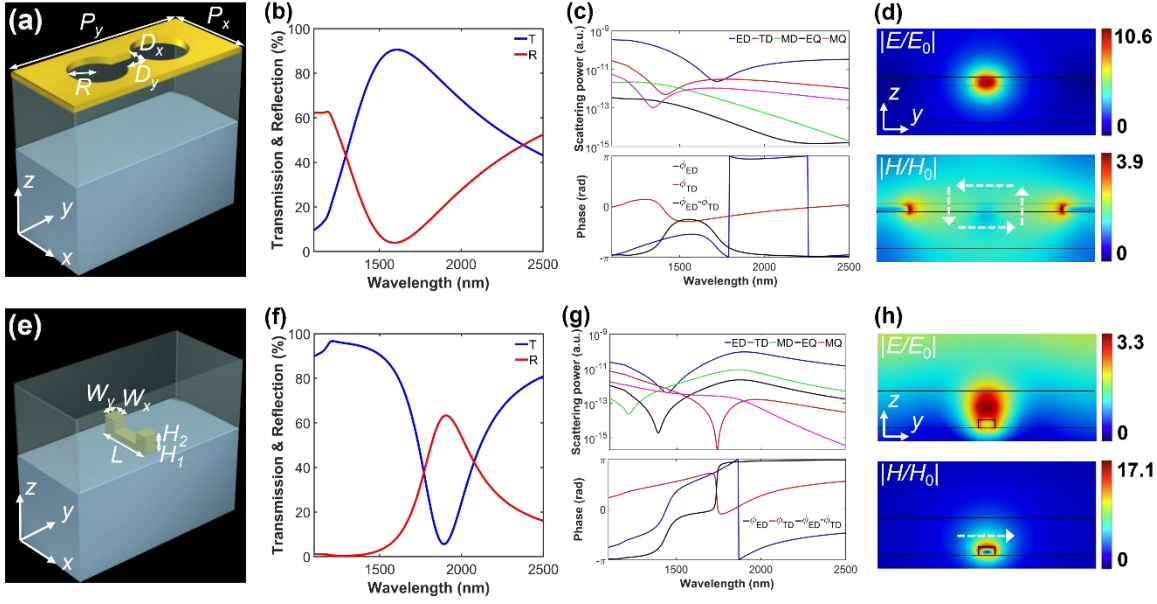
93 **Fig. 1** (a) Schematic diagram of the proposed anapole metamaterial array for refractive index sensing.
94 The inset is the top-view scanning electron microscope image of the fabricated sample. The scale bar is
95 500 nm. (b) Schematic depiction for the excited anapole mode, which originates from the destructive
96 interference between electric dipole (blue arrow) and toroidal dipole (red arrow with pink torus and
97 green circulating magnetic field) moments.
98

99
100 glass layer and covered with a dumbbell-perforated gold film. The perforations (apertures)
101 in the gold film are aligned to the vertical split-ring resonators. The inset of Fig. 1a shows
102 the top-view scanning electron microscope image of the fabricated sample. More details of
103 the fabrication process and scanning electron microscope images can be found in Methods
104 and Supplementary Information. With normal x -polarized plane wave illuminating,
105 circulating currents (pink arrows) in two circular apertures and the vertical split-ring
106 resonator can be induced, which can generate the circulating magnetic field (green arrow)
107 and subsequently excite the x -directed toroidal dipole moments (red arrow) [39, 40], as
108 shown in Fig. 1b. The $-x$ -directed electric dipole moments can also be excited due to the
109 charge oscillations at two central edges of the apertures. When two dipole excitations
110 possess the same intensity but are out of phase, the destructive interference between them

111 leads to the anapole mode, accompanied by the strong field confinement and vanishing far-
112 field radiation.

113 To elaborate on the physical mechanism of the plasmonic anapole metamaterial, we
114 first investigate its two components, the upper dumbbell-perforated gold film and the lower
115 vertical split-ring resonator, whose schematic diagrams of configuration are shown in Fig.
116 2a and e, respectively. Figure 2b gives the transmission and reflection spectra of the
117 dumbbell-perforated gold film placed on the dielectric substrate. A transmission peak of
118 more than 90% can be observed at resonant wavelength $\lambda = 1608$ nm. According to the
119 multipole decomposition (see Supplementary Information for details) in Fig. 2c, this
120 resonant mode is mainly contributed by the electric dipole and toroidal dipole moments,
121 accompanied by a weak magnetic quadrupole (MQ) contribution. Although electric dipole
122 and toroidal dipole moments have a similar amplitude near the resonant wavelength, their
123 phase difference is not close to π , so the resonance here is intrinsically a hybrid mode
124 instead of an anapole mode. The yz -plane field distributions normalized to the incident
125 wave amplitude, at the resonant wavelength, are plotted in Fig. 2d. An electric hotspot
126 emerges at the center of two apertures and a circulating magnetic field (white dashed
127 arrows) can be observed, which exhibits the characteristics of both electric dipole and
128 toroidal dipole distributions and thus offers the possibility for anapole excitation [25].

129 Figure 2f shows the spectra of the vertical split-ring resonator suspended in a spin on
130 glass layer. A transmission dip of around 10% indicates that the resonance is excited at
131 wavelength $\lambda = 1892$ nm. The main components of the excitation are a dominant electric
132 dipole moment as well as weak magnetic dipole (MD) and electric quadrupole (EQ)
133 moments, as shown in Fig. 2g. This configuration does not constitute an anapole mode in



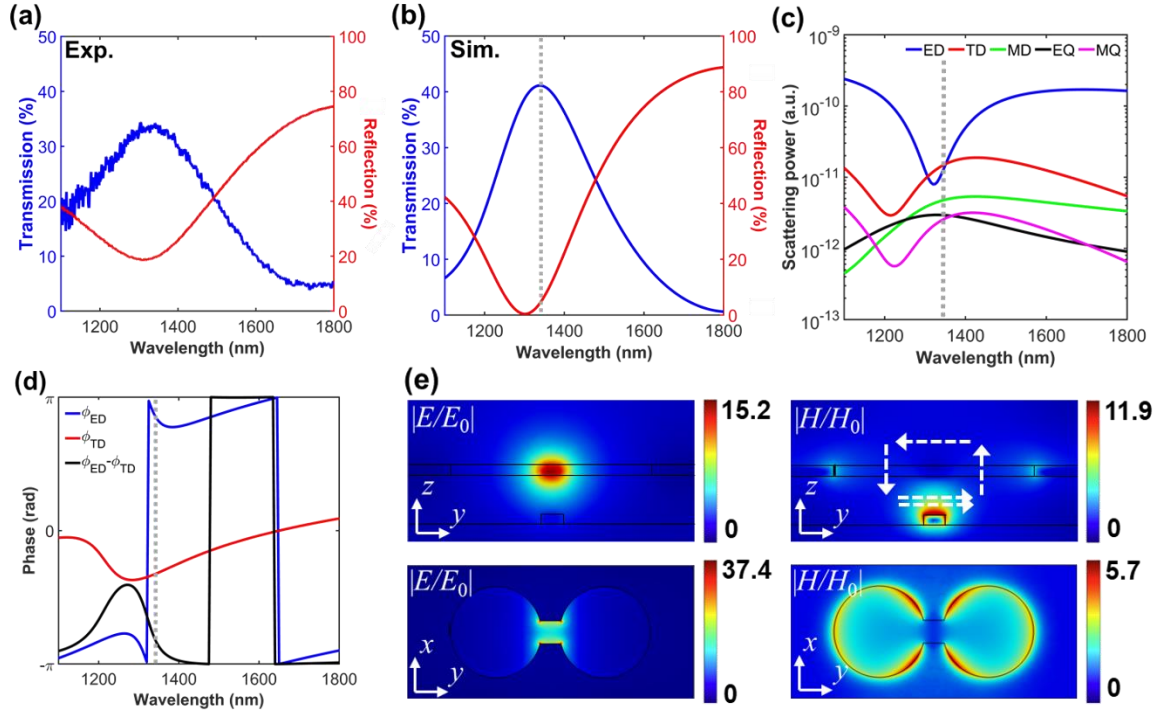
135 **Fig. 2** Electromagnetic responses of two components of the plasmonic anapole metamaterial. (a)
136 Schematic diagram of the configuration, (b) transmission (blue curve) and reflection (red curve) spectra,
137 (c) multipole decomposition and phases of electric dipole and toroidal dipole moments, and (d)
138 normalized yz -plane electric field and magnetic field distributions of the dumbbell-perforated gold film
139 placed on the dielectric substrate. The field distribution is extracted from the corresponding resonant
140 wavelength. White dashed arrows depict the orientations of the magnetic field. (e), (f), (g) and (h) Those
141 for the vertical split-ring resonator suspended in a spin on glass layer. Feature sizes: $P_x = 380$ nm, $P_y =$
142 820 nm, $R = 130$ nm, $D_x = 65$ nm, $D_y = 60$ nm, $L = 270$ nm, $W_x = 60$ nm, $W_y = 60$ nm, $H_1 = 30$ nm, H_2
143 = 55 nm, and thicknesses of the perforated gold film and the spin on glass film are 30 nm and 135 nm,
144 respectively.

145

146 the desired spectral range because the similar amplitude and the opposite phase for electric
147 dipole and toroidal dipole moments do not appear simultaneously. The normalized field
148 distributions are presented in Fig. 2h. The electric hotspot and magnetic hotspot can be
149 found in the center of the vertical split-ring resonator, indicating the excitations of both
150 electric dipole and magnetic dipole moments [41-44]. The electric hotspot of the vertical

151 split-ring resonator can effectively overlap that of the dumbbell-perforated gold film, and
152 the magnetic hotspot of the vertical split-ring resonator can boost the circulating magnetic
153 field of the dumbbell-perforated gold film due to their similar orientations in the spin on
154 glass layer. Although the anapole mode cannot be directly acquired in the single component,
155 combining two components provides the conditions for the anapole excitation.
156 Consequently, combining these two components can generate efficient coupling between
157 them and enhance the electric dipole and toroidal dipole moments simultaneously, which
158 is expected to provide the opportunity for a strong anapole response.

159 To verify the analysis above, we experimentally and numerically demonstrate the
160 plasmonic anapole metamaterial combining both dumbbell-perforated gold film and
161 vertical split-ring resonator components. Since the device performance is dominated by the
162 physical mechanism of anapole mode instead of optimized parameters, the geometric
163 parameters selection is mainly based on the mechanism of anapole excitation and the
164 fabrication precision. The experimentally measured transmission and reflection spectra are
165 plotted in Fig. 3a. The transmission peak representing the resonance can be observed at
166 wavelength $\lambda = 1340$ nm, showing a blue shift compared to the resonant wavelengths of
167 two components (1608 nm and 1892 nm). That is because the involvement of the other
168 component introduces not only new material but also effective coupling between two
169 components. The measured line shape of the transmission and reflection spectra agree well
170 with the simulated results in Fig. 3b. The slight difference in the peak values of
171 transmission and reflection, as well as a broader line width in the experimental
172 measurements, are expected due to inevitable variations in metamaterial dimensions and
173 imperfections with the fabricated sample.



174

175 **Fig. 3** Electromagnetic responses of the plasmonic anapole metamaterial. (a) Measured and (b)
176 simulated transmission (blue curve) and reflection (red curve) spectra, (c) multipole decomposition, (d)
177 phases of electric dipole and toroidal dipole moments, and (e) normalized electric field and magnetic
178 field distributions of the plasmonic anapole metamaterial in the yz -plane and the xy -plane. Grey dotted
179 lines in Fig. 3b-d denote the resonant wavelength of anapole mode. White dashed arrows depict the
180 orientations of the magnetic field. The xy cut plane is located in the middle of the upper dumbbell-
181 perforated gold film. All the geometric parameters are identical to those in Fig. 2.

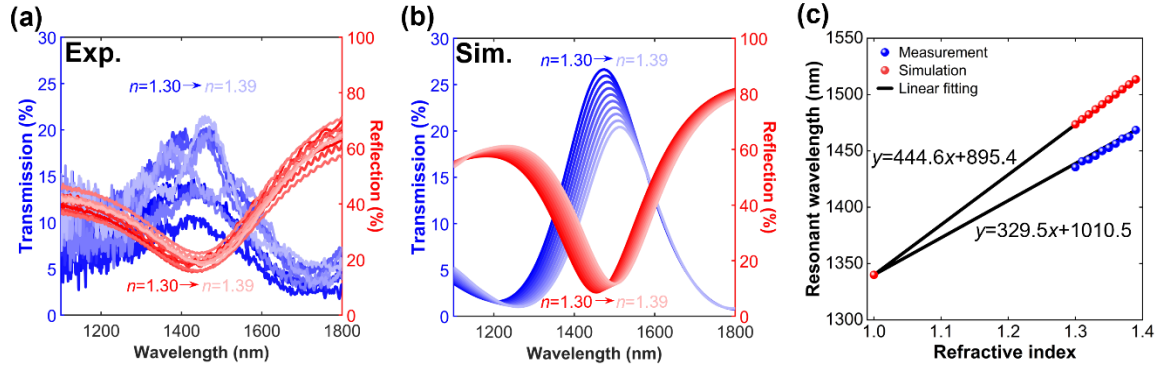
182

183 Figure 3c and d depict the multipole decomposition and phases of electric dipole and
184 toroidal dipole moments of the plasmonic anapole metamaterial, respectively. Electric
185 dipole and toroidal dipole moments have similar amplitudes and approximately opposite
186 phases at the wavelength around $\lambda = 1340$ nm (grey dotted lines), implying the effective
187 excitation of the anapole mode. It is interesting to point out that the slight deviation of
188 phase difference from $-\pi$ results from the involved additional loss of gold (See Methods

189 and Supplementary Information), which will not influence the mechanism of anapole
190 excitation. The electromagnetic field distributions are given in Fig. 3e. The electric hotspot
191 is located at the center of dumbbell-perforated gold film and the magnetic hotspots emerge
192 at two aperture edges and in the center of the vertical split-ring resonator, which
193 simultaneously inherits the properties of both dumbbell-perforated gold film and vertical
194 split-ring resonator.

195 We now turn our attention to the sensitivity of metamaterial's resonant mode to the
196 ambient refractive index. In the case of the metamaterial considered here, the toroidal
197 dipole moment is parallel to the direction of the incident electric field, which offers stronger
198 interactions between light and matter than that is perpendicular [24, 25]. Moreover,
199 according to the field distributions in Fig. 3e, the electric hotspot is exposed to the
200 environment, resulting in a strong interaction between hotspot and sensing medium and
201 subsequently a high sensitivity to the ambient refractive index variations. In contrast, for
202 dielectric anapole metamaterials and metasurfaces reported in the literature, the
203 electromagnetic field remains hidden within the dielectric, limiting the practical utility of
204 these devices [45, 46].

205 Benefiting from the effective coupling between two components and the subsequent
206 anapole mode, the maximum electric field enhancement factor $|E/E_0| = 15.2$ in yz plane is
207 larger than those of only dumbbell-perforated gold film ($|E/E_0| = 10.6$) and only vertical
208 split-ring resonator ($|E/E_0| = 3.3$). Moreover, as shown in Fig. 3b, the simulated line width
209 of the plasmonic anapole metamaterial is reduced to 295 nm, which is smaller than those
210 of only dumbbell-perforated gold film (1137 nm) and vertical split-ring resonator (404 nm).
211 These advantages are expected to efficiently promote sensing performance. It should be



212

213 **Fig. 4** Refractive index sensing application of the plasmonic anapole metamaterial. (a) Measured and
 214 (b) simulated transmission and reflection spectra with variable ambient refractive index from 1.30 to
 215 1.39 with a step of 0.01. Dark (light) blue and red correspond to transmission and reflection at refractive
 216 index $n = 1.30$ (1.39). (c) The resonant wavelengths of the anapole mode from experimental and
 217 simulation results as functions of the ambient refractive index. The black solid lines represent the linear
 218 fitting results.

219

220 noted that the magnetic field enhancement $|H/H_0| = 11.9$ is smaller than that of only the
 221 vertical split-ring resonator because of the unavoidable influence of the upper dumbbell-
 222 perforated gold film. Since the magnetic hotspot is located in the spin on glass layer, its
 223 impact on sensitivity will be reduced.

224 To investigate and examine the sensing performance of the plasmonic anapole
 225 metamaterial, we deposit the oil with a refractive index from 1.30 to 1.39 with a step of
 226 0.01 onto the sample. Figure 4a shows the measured transmission and reflection spectra
 227 with variable ambient refractive index. With the ambient refractive index varying from 1.30
 228 to 1.39, the measured resonant wavelength redshifts from 1435.5 nm to 1468.5 nm. The
 229 simulated result in Fig. 4b is in good agreement with the measured one, indicating a redshift
 230 of the resonant wavelength from 1473.5 nm to 1513.4 nm without changing the line shape.
 231 These two results both show the linear relationship between the resonant wavelength and

232 refractive index, which is consistent with the theoretical model [47]. The small difference
233 between these two results is due to the roughness of the sample. As a key performance of
234 the sensor, the sensitivity $\Delta\lambda/\Delta n$ defined as the spectral shift per refractive index unit (RIU)
235 is studied in Fig. 4c. By employing a linear fitting, the sensitivities of measurement and
236 simulation results are around 330 nm/RIU and 445 nm/RIU, respectively, which are
237 comparative to conventional plasmonic refractive index sensors by LSPR [5, 13, 15, 48].
238 The proposed anapole metamaterial sensor can acquire an effective transmission channel
239 due to the nonradiative property, which is beneficial to practical low-loss meta-devices.
240 Considering the infrared spectrometer resolution of around 28.7 pm, the experimental
241 detection limit $\Delta n_{\text{limit}} = \Delta\lambda_{\text{limit}}/\text{Sensitivity} = 8.7 \times 10^{-5}$ RIU can be obtained.

242 In addition, to analyze the influence of ambient refractive index on the multipole
243 contribution and thus the anapole mode, the multipole decompositions and phases of
244 electric dipole and toroidal dipole moments with different ambient refractive index are
245 given in the Supplementary Information. The contributions of electric dipole and toroidal
246 dipole moments and their phase differences keep nearly constant except for a redshift,
247 which demonstrates that the proposed plasmonic anapole metamaterial can work in a wide
248 range of refractive index and provides a novel method of adjusting the ambient refractive
249 index to flexibly manipulate the anapole mode.

250

251 Conclusion

252 To conclude, we have demonstrated the plasmonic metamaterial with anapole response and
253 its application in refractive index sensing. By analyzing the spectra, multipole
254 decompositions and field distributions of the upper dumbbell-perforated gold film and the

255 lower vertical split-ring resonator, we demonstrate that the anapole mode cannot be directly
256 excited in a single component, while they can provide efficient electric dipole and toroidal
257 dipole moments and effectively couple with each other, which are desirable for the anapole
258 response. After the combination of these two components, an anapole mode at around 1340
259 nm with a stronger electric field enhancement factor of 15.2 and a narrower line width of
260 295 nm can be achieved. Benefiting from these characteristics, the sensitivities of the
261 plasmonic anapole-based refractive index sensor are 330 nm/RIU and 445 nm/RIU in
262 experiment and simulation, respectively. Considering the infrared spectrometer resolution,
263 the experimental detection limit of 8.7×10^{-5} RIU is obtained. Apart from sensing
264 application, this work opens new paths for manipulating the plasmonic anapole mode by
265 varying ambient refractive index and facilitates its applications in spectroscopy and optical
266 nonlinearity.

267

268 **Methods**

269 **Metamaterial nanofabrication**

270 First, a ZEP520A layer was spin-coated at 4000 rpm onto a fused silica substrate and baked
271 for 5 min at 180 °C. An Spacer layer was spin-coated at 1500 rpm onto the ZEP520A layer
272 to reduce the positional error during the e-beam exposure. The base rod and two prongs of
273 vertical split-ring resonator were fabricated by successive two e-beam exposures and lift-
274 off processes. Then, a spin on glass layer isolating the dumbbell-perforated gold film and
275 vertical split-ring resonator was spin-coated at 3000 rpm onto the fused silica substrate
276 with fabricated vertical split-ring resonator and baked for 3 min at 200 °C. Its thickness of
277 135 nm was acquired by the reactive ion etching (RIE). Last, 30 nm gold films were

278 deposited by RF sputter, and the antietch layer (ZEP520A) was spin-coated onto the gold
279 film. The dumbbell-shaped holes in the same area were processed by e-beam exposure and
280 fabricated by the RIE process.

281

282 **Optical measurement**

283 Bruker VERTEX 70 Fourier-transform infrared spectrometer equipped with Bruker
284 HYPERION 2000 infrared microscope was exploited to measure the spectrum data. An
285 aperture was employed to collect the incidence to a square area of about $150 \times 150 \mu\text{m}^2$,
286 which is the same as the size of the fabricated sample. The transmission and reflection
287 spectra were normalized by those of the fused silica substrate and the gold mirror.
288 Refractive index sensing is performed by placing a drop of oil with a certain refractive
289 index (Cargille oils Series AAA), measuring the transmission and reflection spectra of the
290 metamaterial, rinsing the sample in methanol, drying, and repeating again. The thickness
291 of oil layer is more than $100 \mu\text{m}$ to ensure the sample area can be entirely covered, which
292 is far larger than sample thickness and wavelength, and the influence of oil thickness can
293 thus be ignored.

294

295 **Numerical simulation**

296 Electromagnetic responses of the metamaterial were numerically simulated by commercial
297 software COMSOL Multiphysics based on the finite element method. Perfectly matched
298 layers (PMLs) at the top and bottom of the metamaterial were used to truncate the open
299 space. Periodic boundary conditions were employed in x and y directions to simulate the
300 periodic array. Due to the large thickness of the oil layer, it is simulated as the background

301 media above the metamaterial. The maximum mesh element size is less than 1/10 of the
302 wavelength, and the resolution of narrow regions is larger than 2. The refractive indexes of
303 the fused silica substrate and spin on glass layer were 1.4584 and 1.41, respectively. The
304 permittivity of gold was described by the Lorentz-Drude model with a plasma frequency
305 of 8.997 eV and a damping coefficient of 0.07 eV. As the wavelength is shorter than 1800
306 nm, an additional imaginary part of the permittivity of gold was involved to consider the
307 higher experimental loss at the shorter wavelength (see Supplementary Information).

308

309 **Abbreviations**

310 SPP surface plasmon polariton
311 LSPR localized surface plasmon resonance
312 FOM figure-of-merit
313 ED electric dipole
314 TD toroidal dipole
315 MQ magnetic quadrupole
316 MD magnetic dipole
317 EQ electric quadrupole
318 RIU refractive index unit
319 RIE reactive ion etching
320 PML perfectly matched layer

321

322 **Supplementary Information**

323 The online version contains supplementary material available at <https://doi.org/>.

324 **Additional file 1: Figure S1.** (a) Fabrication process and (b) tilt-viewed scanning electron
325 microscope image of the plasmonic anapole metamaterial. **Figure S2.** (a) Transmission and
326 (b) reflection measurement systems. **Figure S3.** Additional imaginary part of the
327 permittivity of gold involved to consider the higher experimental loss at the shorter
328 wavelength. **Figure S4.** Dependences of (a) transmission and (b) reflection spectra for the
329 plasmonic anapole metamaterial on the thickness of spin on glass. **Figure S5.** (a)
330 Transmission (blue curve) and reflection (red curve) spectra and (b) normalized electric
331 field distributions in the yz -plane with the lower vertical split-ring resonator shifts in x -
332 direction $\Delta x = 10$ nm, 20 nm, and 50 nm, respectively. (c) and (d) Those with the y -direction
333 shifts. **Figure S6.** (a) Multipole decompositions and (b) phases of electric dipole and
334 toroidal dipole moments of the plasmonic anapole metamaterial with ambient refractive
335 indexes of 1.30, 1.35 and 1.39.

336

337 **Acknowledgements**

338 The authors acknowledge support from University of Southampton, Nanyang
339 Technological University, and City University of Hong Kong.

340 **Authors' contributions**

341 J.Y., J.Y.O., V.S., N.I.Z, and D.P.T. conceived the idea and designed the experiments. J.Y.,
342 V.S. M.K.C., and H.Y.K. designed the samples and performed the theoretical simulations.
343 J.Y.O., V.S., and H.Y.K. developed the technology and fabricated the samples. J.Y.O. and
344 H.Y.K. performed the inspections of the samples and the optical measurements. J.Y. and
345 M.K.C. performed the data analysis. J.Y., J.Y.O., V.S., M.K.C., N.I.Z, and D.P.T.
346 discussed and prepared the manuscript, and all authors reviewed it. N.I.Z and D.P.T.

347 initiated and supervised the research.

348 **Funding**

349 This work is supported by the UK Engineering and Physical Science Research Council
350 (grants EP/M009122/1 and EP/T02643X/1), the Royal Society (grant IEC/R3/170092), the
351 European Research Council (Advanced Grant No. FLEET-786851), the Singapore
352 Ministry of Education (N.I.Z.; grant MOE2016-T3-1-006), the University Grants
353 Committee / Research Grants Council of the Hong Kong Special Administrative Region,
354 China (Project No. AoE/P-502/20 and GRF Project: 15303521), the Shenzhen Science and
355 Technology Innovation Commission (Grant No. SGDX2019081623281169), the
356 Department of Science and Technology of Guangdong Province (2020B1515120073), and
357 the City University of Hong Kong (Grant No. 9380131).

358 **Availability of data and materials**

359 The data that support the findings of this study are openly available in University of
360 Southampton ePrints research repository at <https://doi.org/10.5258/SOTON/D2387>

361 **Declarations**

362 **Competing interests**

363 The authors declare that they have no competing interests.

364

365 **References**

- 366 1. Altug H, Oh SH, Maier SA, Homola J, Advances and applications of nanophotonic
367 biosensors. Nat Nanotechnol. 2022;17:5-16.
- 368 2. Tseng ML, Jahani Y, Leitis A, Altug H, Dielectric Metasurfaces Enabling Advanced
369 Optical Biosensors. ACS Photonics. 2020;8:47-60.

- 370 3. Ahmadvand A, Gerislioglu B, Photonic and Plasmonic Metasensors. *Laser Photonics*
371 *Rev.* 2021;16:2100328.
- 372 4. Park J-H, Ndao A, Cai W, Hsu L, Kodigala A, Lepetit T, Lo Y-H, Kanté B, Symmetry-
373 breaking-induced plasmonic exceptional points and nanoscale sensing. *Nat Phys.*
374 2020;16:462-8.
- 375 5. Nugroho FAA, Albinsson D, Antosiewicz TJ, Langhammer C, Plasmonic Metasurface
376 for Spatially Resolved Optical Sensing in Three Dimensions. *ACS Nano.* 2020;14:2345-
377 53.
- 378 6. You JW, Ma Q, Lan Z, Xiao Q, Panoiu NC, Cui TJ, Reprogrammable plasmonic
379 topological insulators with ultrafast control. *Nat Commun.* 2021;12:5468.
- 380 7. Liu C, Ma Q, Luo ZJ, Hong QR, Xiao Q, Zhang HC, Miao L, Yu WM, Cheng Q, Li L,
381 A programmable diffractive deep neural network based on a digital-coding metasurface
382 array. *Nat Electron.* 2022;5:113-22.
- 383 8. Allison G, Sana AK, Ogawa Y, Kato H, Ueno K, Misawa H, Hayashi K, Suzuki H, A
384 Fabry-Perot cavity coupled surface plasmon photodiode for electrical biomolecular sensing.
385 *Nat Commun.* 2021;12:6483.
- 386 9. Shen Y, He K, Zou Q, Xing S, Huang J, Zheng M, She X, Jin C, Ultrasmooth Gold
387 Nanogroove Arrays: Ultranarrow Plasmon Resonators with Linewidth down to 2 nm and
388 Their Applications in Refractive Index Sensing. *Adv Funct Mater.* 2021;32:2108741.
- 389 10. Kabashin AV, Evans P, Pastkovsky S, Hendren W, Wurtz GA, Atkinson R, Pollard R,
390 Podolskiy VA, Zayats AV, Plasmonic nanorod metamaterials for biosensing. *Nat Mater.*
391 2009;8:867-71.
- 392 11. Sreekanth KV, Alapan Y, ElKabbash M, Ilker E, Hinczewski M, Gurkan UA, De Luca

- 393 A, Strangi G, Extreme sensitivity biosensing platform based on hyperbolic metamaterials.
- 394 Nat Mater. 2016;15:621-7.
- 395 12. Xu Y, Bai P, Zhou X, Akimov Y, Png CE, Ang LK, Knoll W, Wu L, Optical Refractive
- 396 Index Sensors with Plasmonic and Photonic Structures: Promising and Inconvenient Truth.
- 397 Adv Opt Mater. 2019;7:1801433.
- 398 13. Wu PC, Liao CY, Chen J-W, Tsai DP, Isotropic Absorption and Sensor of Vertical Split-
- 399 Ring Resonator. Adv Opt Mater. 2017;5:1600581.
- 400 14. Gerislioglu B, Dong L, Ahmadvand A, Hu H, Nordlander P, Halas NJ, Monolithic
- 401 Metal Dimer-on-Film Structure: New Plasmonic Properties Introduced by the Underlying
- 402 Metal. Nano Lett. 2020;20:2087-93.
- 403 15. Wu PC, Sun G, Chen WT, Yang K-Y, Huang Y-W, Chen Y-H, Huang HL, Hsu W-L,
- 404 Chiang HP, Tsai DP, Vertical split-ring resonator based nanoplasmonic sensor. Appl Phys
- 405 Lett. 2014;105:033105.
- 406 16. Ahmed R, Ozen MO, Karaaslan MG, Prator CA, Thanh C, Kumar S, Torres L, Iyer N,
- 407 Munter S, Southern S, Henrich TJ, Inci F, Demirci U, Tunable Fano-Resonant
- 408 Metasurfaces on a Disposable Plastic-Template for Multimodal and Multiplex Biosensing.
- 409 Adv Mater. 2020;32:1907160.
- 410 17. Liang Y, Koshelev K, Zhang F, Lin H, Lin S, Wu J, Jia B, Kivshar Y, Bound States in
- 411 the Continuum in Anisotropic Plasmonic Metasurfaces. Nano Lett. 2020;20:6351-6.
- 412 18. Chen H, Wang H, Wong KY, Lei D, High-Q localized surface plasmon resonance based
- 413 on bound states in the continuum for enhanced refractive index sensing. Opt Lett.
- 414 2022;47:609-12.
- 415 19. Cetin AE, Altug H, Fano resonant ring/disk plasmonic nanocavities on conducting

- 416 substrates for advanced biosensing. *ACS Nano*. 2012;6:9989-95.
- 417 20. Wang J, Kühne J, Karamanos T, Rockstuhl C, Maier SA, Tittl A, All-Dielectric
- 418 Crescent Metasurface Sensor Driven by Bound States in the Continuum. *Adv Funct Mater*.
- 419 2021;31:2104652.
- 420 21. Zhou Y, Guo Z, Zhao X, Wang F, Yu Z, Chen Y, Liu Z, Zhang S, Sun S, Wu X, Dual-
- 421 Quasi Bound States in the Continuum Enabled Plasmonic Metasurfaces. *Adv Opt Mater*.
- 422 2022;2200965.
- 423 22. Baryshnikova KV, Smirnova DA, Luk'yanchuk BS, Kivshar YS, Optical Anapoles:
- 424 Concepts and Applications. *Adv Opt Mater*. 2019;7:1801350.
- 425 23. Yang Y, Bozhevolnyi SI, Nonradiating anapole states in nanophotonics: from
- 426 fundamentals to applications. *Nanotechnology*. 2019;30:204001.
- 427 24. Fedotov VA, Rogacheva AV, Savinov V, Tsai DP, Zheludev NI, Resonant transparency
- 428 and non-trivial non-radiating excitations in toroidal metamaterials. *Sci Rep*. 2013;3:2967.
- 429 25. Wu PC, Liao CY, Savinov V, Chung TL, Chen WT, Huang YW, Wu PR, Chen YH, Liu
- 430 AQ, Zheludev NI, Tsai DP, Optical Anapole Metamaterial. *ACS Nano*. 2018;12:1920-7.
- 431 26. Miroshnichenko AE, Evlyukhin AB, Yu YF, Bakker RM, Chipouline A, Kuznetsov AI,
- 432 Luk'yanchuk B, Chichkov BN, Kivshar YS, Nonradiating anapole modes in dielectric
- 433 nanoparticles. *Nat Commun*. 2015;6:8069.
- 434 27. Semmlinger M, Zhang M, Tseng ML, Huang TT, Yang J, Tsai DP, Nordlander P, Halas
- 435 NJ, Generating Third Harmonic Vacuum Ultraviolet Light with a TiO₂ Metasurface. *Nano*
- 436 *Lett*. 2019;19:8972-8.
- 437 28. Yao J, Li B, Cai G, Liu QH, Doubly mirror-induced electric and magnetic anapole
- 438 modes in metal-dielectric-metal nanoresonators. *Opt Lett*. 2021;46:576-9.

- 439 29. Gurvitz EA, Ladutenko KS, Dergachev PA, Evlyukhin AB, Miroshnichenko AE,
440 Shalin AS, The High-Order Toroidal Moments and Anapole States in All-Dielectric
441 Photonics. *Laser Photonics Rev.* 2019;13:1800266.
- 442 30. Ospanova AK, Stenishchev IV, Basharin AA, Anapole Mode Sustaining Silicon
443 Metamaterials in Visible Spectral Range. *Laser Photonics Rev.* 2018;12:1800005.
- 444 31. Hernandez-Sarria JJ, Oliveira ON, Mejia-Salazar JR, Toward Lossless Infrared Optical
445 Trapping of Small Nanoparticles Using Nonradiative Anapole Modes. *Phys Rev Lett.*
446 2021;127:186803.
- 447 32. Hüttenhofer L, Tittl A, Kühner L, Cortés E, Maier SA, Anapole-Assisted Absorption
448 Engineering in Arrays of Coupled Amorphous Gallium Phosphide Nanodisks. *ACS*
449 *Photonics.* 2021;8:1469-76.
- 450 33. Kuznetsov AI, Evlyukhin AB, Gonçalves MR, Reinhardt C, Koroleva A, Arnedillo ML,
451 Kiyan R, Marti O, Chichkov BN, Laser fabrication of large-scale nanoparticle arrays for
452 sensing applications. *ACS Nano.* 2011;5:4843-9.
- 453 34. Jeong J, Goldflam MD, Campione S, Briscoe JL, Vabishchevich PP, Nogaj J, Sinclair
454 MB, Luk TS, Brener I, High Quality Factor Toroidal Resonances in Dielectric
455 Metasurfaces. *ACS Photonics.* 2020;7:1699-707.
- 456 35. Wang W, Srivastava YK, Gupta M, Wang Z, Singh R, Photoswitchable Anapole
457 Metasurfaces. *Adv Opt Mater.* 2021;10:2102284.
- 458 36. Liu X, Liu Z, Hua M, Wang L, Wang K, Zhang W, Ning Y, Shi Y, Wang X, Yang F,
459 Tunable Terahertz Metamaterials Based on Anapole Excitation with Graphene for
460 Reconfigurable Sensors. *ACS Applied Nano Materials.* 2020;3:2129-33.
- 461 37. Savinov V, Papasimakis N, Tsai DP, Zheludev NI, Optical anapoles. *Commun Phys.*

- 462 2019;2:1-4.
- 463 38. Wu J, Li Z, Li M, Wang Y, Plasmonic refractive index sensing enhanced by anapole
464 modes in metal-dielectric nanostructure array. *J Opt.* 2021;23:035002.
- 465 39. Kaelberer T, Fedotov V, Papasimakis N, Tsai D, Zheludev N, Toroidal dipolar response
466 in a metamaterial. *Science.* 2010;330:1510-2.
- 467 40. Papasimakis N, Fedotov VA, Savinov V, Raybould TA, Zheludev NI, Electromagnetic
468 toroidal excitations in matter and free space. *Nat Mater.* 2016;15:263-71.
- 469 41. Wu PC, Chen WT, Yang K-Y, Hsiao CT, Sun G, Liu AQ, Zheludev NI, Tsai DP,
470 Magnetic plasmon induced transparency in three-dimensional metamolecules.
471 *Nanophotonics.* 2012;1:131-8.
- 472 42. Chen CC, Hsiao CT, Sun S, Yang K-Y, Wu PC, Chen WT, Tang YH, Chau Y-F, Plum
473 E, Guo G-Y, Fabrication of three dimensional split ring resonators by stress-driven
474 assembly method. *Opt Express.* 2012;20:9415-20.
- 475 43. Chan H-C, Sun S, Guo G-Y, Near-infrared left-handed metamaterials made of arrays
476 of upright split-ring pairs. *J Phys D: Appl Phys.* 2018;51:265103.
- 477 44. Tsai WY, Chung TL, Hsiao HH, Chen JW, Lin RJ, Wu PC, Sun G, Wang CM, Misawa
478 H, Tsai DP, Second Harmonic Light Manipulation with Vertical Split Ring Resonators. *Adv
479 Mater.* 2019;31:1806479.
- 480 45. Zanganeh E, Evlyukhin A, Miroshnichenko A, Song M, Nenasheva E, Kapitanova P,
481 Anapole Meta-Atoms: Nonradiating Electric and Magnetic Sources. *Phys Rev Lett.*
482 2021;127:096804.
- 483 46. Yang Y, Zenin VA, Bozhevolnyi SI, Anapole-Assisted Strong Field Enhancement in
484 Individual All-Dielectric Nanostructures. *ACS Photonics.* 2018;5:1960-6.

485 47. Zhu J, Zhang L, Jiang S, Ou J-Y, Liu QH, Selective light trapping of plasmonic stack
486 metamaterials by circuit design. *Nanoscale*. 2020;12:2057-62.

487 48. Ray D, Raziman TV, Santschi C, Etezadi D, Altug H, Martin OJF, Hybrid Metal-
488 Dielectric Metasurfaces for Refractive Index Sensing. *Nano Lett*. 2020;20:8752-9.

489